Full Text View

Volume 32, Issue 11 (November 2002)

Journal of Physical Oceanography
Article: pp. 2977–2987 | Abstract | PDF (1.63M)

Phase Distribution of Small-Scale Ocean Surface Roughness*

Paul A. Hwang

Oceanography Division, Naval Research Laboratory, Stennis Space Center, Mississippi

(Manuscript received July 20, 2001, in final form November 14, 2001)

DOI: 10.1175/1520-0485(2002)032<2977:PDOSSO>2.0.CO;2

ABSTRACT

Remote sensing is becoming an important tool for oceanographic research. As the resolution of remote sensors is becoming comparable to the wavelength of dominant ocean surface waves, the usual assumption of homogeneous surface roughness is no longer adequate. In this paper, laboratory data of surface wave displacement and small-scale surface roughness (wavelength 0.004–0.10 m) measured by a scanning slope sensor are analyzed. The results show that higher intensity of surface roughness occurs at the upwind quadrant of the wave crests of background waves. Over a wide wind speed range, the maximum surface roughness is located close to the maximum of surface velocity divergence.

Table of Contents:
- Introduction
- Scanning slope measurement
- Analysis of phase distribution
- Discussion and conclusions
- REFERENCES
- APPENDIX
- FIGURES

1. Introduction

Small-scale surface waves serve as the roughness elements that affect the propagation and scattering of optical waves and microwaves at the ocean surface. For Ku- and X-band radars, the resonant wavelengths are a few centimeters. These short waves are easily generated by wind and modified by surface currents from all sources. They serve as natural tracers for remote sensing of oceanographic processes. For example, remote sensing of internal and surface waves is based primarily on measuring the modulation of the radar-resonant waves by the surface currents induced by the internal or surface waves (e.g., Wright 1966, 1968; Hughes 1978; Hughes and Grant 1978; Hughes and Gower 1983; Thompson and Gasparovic 1986; Hughes and Dawson 1988; Thompson 1988). For optical remote sensing, surface waves of a wide range of length scales, from capillary waves of several millimeters to gravity waves of several decameters, also contribute to enhanced irradiance observed in the upper ocean (e.g., Zaneveld et al. 2001a,b).

Presently, in theoretical treatments of scattering and radiation problems, it is generally assumed that the small-scale

roughness on the ocean surface is uniformly distributed. This is a reasonable assumption when the footprint of the sensor is large. As the spatial resolution of remote sensors is reaching decameter or even submeter scales, the homogeneous assumption becomes inadequate. Preferential presence of short waves near the crests of background waves is obvious even to casual observers. One of the well-documented observations is the parasitic capillary waves phase locked with short and steep gravity waves (e.g., Cox 1958; Ebuchi et al. 1987; Perlin et al. 1993; Fedorov and Melville 1998; Jiang et al. 1999). Longuet-Higgins (1963, 1992, 1995) presents theoretical analyses describing the physical mechanism that produces this phenomenon. The steep curvature near the crest of the short gravity waves produces localized surface tension force that serves as generator of capillary waves. These capillary waves decay very fast and the evolution processes are frequently completed at the front phase of the short wave crest.

If the length scale of the underlying waves is much longer than a few decimeters and the waves do not have the high curvature necessary to produce localized capillary waves, it is less clear what is the resulting phase distribution of the riding short waves. In the absence of wind forcing, Longuet-Higgins (1960) shows that short gravity waves become steeper and shorter at the crest of long waves, and lower and longer at the long wave troughs. The mechanism is identified to be the work done by the long waves against the radiation stress of the short waves. When wind forcing is involved, the contributions from wind generation, curvature generation, and long wave–short wave interaction become very complicated. The relaxation model based on action density conservation consideration is generally applied in the numerical calculations of hydrodynamic modulation of short waves by surface currents induced by surface or internal waves (e.g., Keller and Wright 1975; Hughes 1978; Hughes and Grant 1978; Alpers and Hasselmann 1978; Thompson and Gasparovic 1986; Hwang and Shemdin 1990). The comparison of numerical results with measurements (mostly with radar backscattering cross sections) is reasonably good for the modulation of longer gravity waves (about 0.3 m, the L-band radar wavelength) but not very satisfactory for shorter waves.

In this paper, laboratory experiments of wind-generated waves riding on mechanically generated background waves are conducted. A scanning slope sensor records the space–time evolution of small-scale waves and a capacitance wave gauge measures the surface displacement. The data are analyzed to investigate the phase distribution of short waves on the background mechanical waves. The experiment is described in section 2. The scanning slope data provide wavenumber resolution, thus the phase distributions of individual wave components as well as the integrated mean square slopes can be quantified. The analysis is described in section 3. Discussions of the results and conclusions are presented in section 4.

2. Scanning slope measurement

To investigate the wavenumber properties of small-scale surface waves, a scanning laser slope sensing technique is developed. The method uses an acousto–optic modulator to steer a laser beam to discrete positions in a predetermined pattern. In the present application, a simple linear segment of 0.12 m is scanned. Because the system design and operating principle have been presented in earlier publications (Hwang et al. 1993; Hwang 1999), only a brief description of the experiment is given here.

The data are acquired in the Air–Sea Interaction Laboratory, University of Delaware. The wind fetch of the measurement station is 16 m, which is near the center of the 1-m-wide wind–wave flume. The water depth and the clearance of the air duct are identically 0.75 m. The scanning slope sensor (SSS) measures the downwind and crosswind slope components over a 0.12-m linear segment along the downwind direction at the center of the flume. The linear segment is sampled at 0.002-m intervals, and the linear scanning pattern is repeated at a rate of 200 Hz. A capacitance wave gauge is placed at the downwind end of the scanning segment and with 0.02-m crosswind offset. The wave gauge sampling is triggered by the SSS pattern repetition signals to achieve synchronization, thus the wave record is sampled at 200 Hz. Two series of experiments are performed: the first series contains wind-generated waves only and the second series contains wind-generated waves on top of background monochromatic waves produced by a mechanical wave generator. The wave height of the background mechanical waves is 0.045 m and the wave period is 1 s. In each series, displacement and slope data of waves generated by eight different wind speeds are collected. The wind friction velocities are calculated from the empirical formula established from earlier measurements conducted in the facility with same settings of water depth and air duct clearance (e.g., Hsu 1981; Sun and Wu 1984; Tseng 1987). The eight wind speeds (wind friction velocities) are 0 (0), 1.98 (0.11), 3.47 (0.18), 5.11 (0.26), 6.78 (0.33), 8.37 (0.43), 9.95 (0.55), and 11.62 (0.68) m s^{-1}. These wind conditions will be referred to as 0 to 7 hereafter. Also, wave breaking becomes visually detectable at wind speeds above 5 m s^{-1} in this facility with the given configurations of water depth and air duct clearance (e.g., Xu et al. 1986; Hwang et al. 1989).

The analysis of the first series of experiment (wind-generated waves only) has been reported by Hwang et al. (1993). The results from the second series of experiment are used to study the modulation characteristics of small-scale waves (Hwang 1999). In the modulation analysis, it is found that the magnitude of modulation can be explained satisfactorily by the relaxation theory (Keller and Wright 1975; Hughes 1978; Alpers and Hasselmann 1978; Hwang and Shemdin 1990) but the phase distribution deviates considerably from theoretical prediction. Here we continue the investigation of the phase distribution.

The high data rate of the SSS output limited the data length (10 s) that could be handled with the computer available at the time of experiment (March 1990). Because of aging, one of the data records (wind condition 3) is corrupted and only 5.4 s of data are recovered. Also, the wave record for the case of mechanical waves only (wind condition 0) is lost and had to be recovered from the space–time series of the scanning slope data. The procedure and its verification are described in appendix A.

3. Analysis of phase distribution

a. Qualitative analysis

Figure 1 displays the space–time images of the downwind wave slope component under eight different wind conditions. For reference, the surface displacement is superimposed on the image. As described in the last section, the wave gauge is placed at the downwind end (x = 0.12 m) of the scanning linear segment, which spans 0.12 m. The phase lag between the two ends of the scanning segment is 27.7° of the background waves. As a visual aid, each mechanical wave record is phase shifted and also plotted at the upwind edge (x = 0 m) of the space–time image of surface slopes. In addition, short line segments with slope $dx/dt = C$ are plotted on the figure at several intervals, where x is the space coordinate, positive downwind; t is time; and C is the phase speed of the mechanical waves. Figure 1 contains a large amount of information on the distribution and evolution of surface roughness composed of small-scale waves. Several qualitative points can be immediately derived:

- The distribution of surface roughness is modulated by the background waves and shows periodic patterns even at very high wind conditions.
- The small-scale waves are concentrated near the crest with slightly higher intensity on the windward quadrant at low wind conditions (waves propagate toward positive x and negative t; thus in the time series plots in Fig. 1, winds and waves come from the right-hand side).
- The propagation speeds of small-scale waves vary significantly along the background waves. In most cases, the propagation speeds are much slower than the phase speed of the background waves. This does not contradict the frequent observation of parasitic capillary waves phase locked at the front of short and steep wave crests (typically with wavelengths on the order of 5–10 cm; e.g., Longuet-Higgins 1992, 1995) that generated the capillary waves. The result merely reflects the fact that those short steep waves are free-propagating waves and travel at speeds much slower than the 1-s background waves used in the experiment. Further discussion on the resonance condition of parasitic capillary waves is presented in appendix B.
- In the absence of wind (wind condition 0), waves much shorter than the background waves are also present. For a better illustration, the case of wind condition 0 is enlarged in Fig. 2, plotted as an intensity image on the top panel and a waterfall plot on the bottom panel. The small disturbances are found on the upstream phase of the background wave crests. The localized roughness distribution highlights the important role the viscous dissipation plays in the evolution of short waves. As illustrated in Fig. 2, the periodic small-scale disturbances are most organized at a location near the wave crest. The source of the small-scale disturbances is most likely the ambient motion of the water surface. A discussion of the spectral properties of ambient motion is presented in appendix C. In the presence of mechanical waves, these disturbances become organized because of modulation by the wave-induced current field. The length scale of the perturbation is very short (Fig. C1) and the small waves decay very quickly (Fig. B2). As a result, the entire episode of each disturbance event occurs almost within the back phase of the wave crest. If dissipation is unimportant, the interaction process evolves through the full wave profile and will result in an in-phase modulation of the amplitude and wavenumber, as in the case of short wave–long wave interaction described by Longuet-Higgins (1960). An alternative interpretation of the generation mechanism of these small ripples is wave-induced wind caused by the orbital velocity of mechanical waves. The amplitude of the orbital velocity is calculated to be 0.16 m s^{-1}, which seems to be quite low for wave generation.

The visual observations presented above clearly show that the distribution of ocean surface roughness (small-scale waves) is not random and homogeneous. The distribution of roughness along background waves displays clear characters of a quasi-deterministic pattern of periodic modulation. Higher roughness occurs at the upwind quadrant of the wave crest. The case of mechanical waves only (wind condition 0) is especially instructive and shows clearly that when small-scale disturbances occur, the higher roughness contributed by short waves occurs at the upstream phase of the background wave crest. Further discussions will be presented after the following quantitative analysis of the phase distribution.

b. Quantitative results

1) WAVENUMBER COMPONENTS

The spatial data offer wavenumber (k) resolution for a more detailed study of the small-scale waves. Using 52 spatial points along the scan line, the 1D wavenumber spectrum is computed for each time step (of 5 ms). The resulting temporal evolution of the spectrum is shown in Fig. 3. To highlight the small-scale wave feature, the curvature spectrum $\chi_{11}(k)$, instead of the slope spectrum $\chi_1(k)$, is presented. The image intensity is proportional to the logarithmic scale of the spectral density. Again, the periodic intensification of wave components due to modulation by background waves is discernable. To further quantify the phase distribution of each wavenumber component, the cross-correlation function between the surface displacement, $\eta(t)$, measured by the wave gauge and the time series of the slope spectral density of a given wavenumber component, $\chi_1(t; k)$, is calculated:

$$R(\tau; k) = \int \eta(t + \tau)\chi_1(t; k)\, dt. \qquad (1)$$

The time lag at the maximum of the correlation function is then converted to the phase angle of the mechanical wave profile. Zero degrees is at the wave crest and a positive angle is toward the forward direction of wave propagation. To compare with the single-point measurement of the surface displacement, the center of the linear scanning segment is used as the phase reference. The results from eight wind conditions for all 26 wavenumber components resolved by the scanning slope sensor (from 60.4 to 1571 rad m^{-1} in equal steps of 60.4 rad m^{-1}) are presented in Fig. 4. For clarity, the top panel shows the results of the first three wind conditions (prior to wave breaking), and the lower panel shows the results of the last five wind conditions (with wave breaking).

These data show that high spectral densities of short waves occur mostly in the windward quadrant of the background wave crest. Three distribution patterns can be identified: windless, low wind and no breaking, and wind waves with breaking. These will be described separately in the following paragraphs.

In the absence of wind (circles in Fig. 4a), very small disturbances are found on the upstream phase of the mechanical wave (Fig. 2). The frequency of the more organized component in these disturbances is estimated from Fig. 2 to be about 14 Hz, very close to f_m, the frequency of minimal phase speed of surface waves. These disturbances propagate much slower than the background waves. As they undergo spatial and temporal evolution, the viscous dissipation modifies the waves, shortening the wavelength and decreasing the amplitude. In the mean time, the divergent surface current field on the upstream phase of the background waves stretches the roughness wavelength allowing the *capacity* for continuous growth of the roughness element. The phase lag curve in Fig. 4 for wind condition 0 (circles) displays several local peaks. The lowest one is somewhat below the wavenumber of minimum phase speed (at k_m = 374 rad m^{-1}) with a phase lag of −46°. The highest peak is at about 700 rad m^{-1} with a phase lag of −44°. For most of the other spectral components, the lag is between −60° and −100°. It is noted that these phase locations are near the maximum of horizontal current divergence (−90°) of the background wave field and suggest that modulation of short waves (0.004–0.10 m in wavelengths) is a much localized process.

For low wind conditions prior to visual wave breaking (Fig. 4a, crosses and pluses), the resulting phase angles of high roughness can be approximately divided into three domains. For longer-scale waves ($60 < k < 300$ rad m^{-1}) high roughness is measured near the wave crests and for shorter waves ($k > 700$ rad m^{-1}) the lag is at −60°. A transitional region is located in the neighborhood of k = 300–700 rad m^{-1}.

When breaking is prominent (Fig. 4b), the phase angles of longer waves ($60 < k < 1000$ rad m^{-1}) vary quite wildly but stay predominantly on the upwind phase of the wind crest. For shorter-scale waves ($k > 1100$ rad m^{-1}), the spreading range of the phase angles decreases and high roughness is observed in the range of +10° to −60°.

2) MEAN SQUARE SLOPES

The temporal evolution of the mean square slopes integrated over the spectral range $60.4 \leq k \leq 1571$ rad m^{-1} (wavelength 0.004–0.104 m) for the eight wind speeds are plotted in Fig. 5. The periodic structure of the mean square slope along the profile of background waves is obvious. The phase angle calculated from the cross correlation between surface displacement and mean square slope is shown in Fig. 6 with the square symbol. Again, the maximum mean square slopes are observed mostly in the upwind quadrant of the wave crest. At low wind speeds ($u_* < 0.2$ m s^{-1}), there is a trend of correlation peak moving closer to the wave crest as wind speed increases. At higher wind speeds, the phase angle decreases and the higher roughness occurs at the upwind phase again.

For comparison, the phase lags of individual wavenumber components as a function of wind friction velocity are also shown in Fig. 6. The 26 wave components are plotted with three different symbols: circles for the first nine components ($k < 544$ rad m^{-1}), crosses for the next nine components ($604 \leq k < 1087$ rad m^{-1}), and pluses for the last eight components ($1148 \leq k < 1571$ rad m^{-1}). The wind speed dependence of the longer wave components, which contribute more to the integrated mean square slope, is similar to the results calculated from the mean square slopes. As shown in Fig. 4a, in the more orderly low wind speed range, the locations of high spectral densities of shorter waves are, in general, farther away from the wave crest for a given wind speed. The basic information about the phase distribution of surface roughness as represented by the two sets of computation (spectral components and mean square slopes) is similar. Both indicate that at low wind or no wind, the intensity of small-scale roughness is higher at a location about −90° on the upwind or upstream phase of the wave crest. The phase lag moves closer to the wave crest as wind speed increases. The trend of phase lag reverses as $u*$ exceeds about 0.25 m^{-1} and higher roughness is located on the upwind quadrant of the wave crest statistically.

4. Discussion and conclusions

Short waves with wavelengths in the millimeter to decimeter range are important roughness elements for optical and microwave remote sensing applications. These waves can be easily modulated by background waves on the ocean surface. The result is an inhomogeneous distribution of the surface roughness. In this paper, the phase distribution of short waves along a regular wave train produced by a mechanical wave generator is investigated. The short water waves are measured by a scanning slope sensor that provides wavenumber resolution to resolve wave components from 0.004 to 0.104 m (wavenumber 60.4–1571 rad m^{-1}) as well as mean square slopes integrated over the wavenumber range. Over a broad wind speed range, it is found that the high roughness intensity occurs on the windward quadrant of the crests of background waves. In the absence of wind forcing, small disturbances from ambient motion of the surface are most organized on the upstream quadrant of the wave crest (Figs. 2 and 6). It is noted that this phase is in the region of surface current divergence. Theoretical analysis of short waves modulation by the orbital currents of long waves indicates that wavelength becomes elongated in the divergent region and contracted in the convergent region (Longuet-Higgins 1960; Keller and Wright 1975; Hughes 1978; Hwang and Shemdin 1990). In general, the spectral density of surface waves tends to increase with wavelength. One explanation of the observed high roughness in the divergent region is that disturbances falling into the divergence region can continue to grow as the wavelength becomes elongated (assuming that whatever mechanism causing the initial disturbances is a continuous process). Because of the highly dissipative nature of short waves, the evolution of the disturbances tends to be very local (appendix B). As a result, higher roughness of ocean surface occurs at the upstream phase of the background wave crests. With wind forcing, the phase of high roughness remains in the windward side but moves closer to the wave crest in low and moderate wind conditions ($u* < \sim 0.25$ m s^{-1}). At higher wind speeds, the phase angle of higher roughness again falls into the upwind quadrant of the long wave crest.

For individual wave components, prior to wave breaking, the phase angle of high slope spectral density of longer waves ($60 < k < 1000$ rad m^{-1}) is near the wave crest with a mild decreasing trend (moving away from the crest toward upwind direction) with increasing wavenumber. For very short waves ($k > 1100$ rad m^{-1}), the phase of high slope spectral density is near −70°. With wave breaking, the phase angle of longer waves varies over a wide range but stays predominately on the upwind phase. For shorter waves under breaking condition, the range extends to between +20° and −60°.

Acknowledgments

This work is sponsored by the Office of Naval Research (Naval Research Laboratory PE 62435N and 61153N). The experiment was conducted at the Air–Sea Interaction Laboratory, University of Delaware, in March 1990. The author is grateful for the hospitality of the Air–Sea Interaction Laboratory. Two anonymous reviewers provided useful comments and suggestions to improve the presentation of the paper. Their help is acknowledged.

REFERENCES

Alpers W., and K. Hasselmann, 1978: The two-frequency microwave technique for measuring ocean wave spectra from an airplane or satellite. *Bound.-Layer Meteor.*, **13**, 215–230. Find this article online

Cox C. S., 1958: Measurements of slopes of high-frequency wind waves. *J. Mar. Res.*, **16**, 199–225. Find this article online

Ebuchi N., H. Kawamura, and Y. Toba, 1987: Fine structure of laboratory wind-wave surface studied using an optical method. *Bound.-Layer Meteor.*, **29**, 133–151. Find this article online

Fedorov A. V., and W. K. Melville, 1998: Nonlinear gravity-capillary waves with forcing and dissipation. *J. Fluid Mech.*, **354**, 1–42. Find

this article online

Hsu L. Y.-H., 1981: Turbulence transfers in the atmospheric surface layer under varied stability conditions—A laboratory study. Ph.D. dissertation, University of Delaware, Lewes, DE, 156 pp.

Hughes B. A., 1978: The effect of internal waves on surface wind waves. 2: Theoretical analysis. *J. Geophys. Res.*, **83**, 455–465. Find this article online

Hughes B. A., and H. L. Grant, 1978: The effect of internal waves on surface wind waves. 1: Experimental measurements. *J. Geophys. Res.*, **83**, 443–454. Find this article online

Hughes B. A., and J. F. R. Gower, 1983: SAR imagery and surface truth comparisons of internal waves in Georgia Strait, British Columbia, Canada. *J. Geophys. Res.*, **88**, 1809–1824. Find this article online

Hughes B. A., and T. W. Dawson, 1988: Joint Canada–U.S. Ocean Wave Investigation Project: An overview of the Georgia Strait Experiment. *J. Geophys. Res.*, **93**, 12219–12234. Find this article online

Hwang P. A., 1999: Microstructure of ocean surface roughness: A study of spatial measurement and laboratory investigation of modulation analysis. *J. Atmos. Oceanic Technol.*, **16**, 1619–1629. Find this article online

Hwang P. A., and O. H. Shemdin, 1990: Modulation of short waves by surface currents—A numerical solution. *J. Geophys. Res.*, **95**, 16311–16318. Find this article online

Hwang P. A., D. Xu, and J. Wu, 1989: Breaking of wind-generated waves: Measurements and characteristics. *J. Fluid Mech.*, **202**, 177–200. Find this article online

Hwang P. A., D. B. Trizna, and J. Wu, 1993: Spatial measurements of short wind waves using a scanning slope sensor. *Dyn. Atmos. Oceans*, **20**, 1–23. Find this article online

Jahne B., and K. S. Riemer, 1990: Two-dimensional wavenumber spectra of small-scale water surface waves. *J. Geophys. Res.*, **95**, 11531–11546. Find this article online

Jiang L., H.-J. Lin, W. W. Schultz, and M. Perlin, 1999: Unsteady ripple generation on steep gravity–capillary waves. *J. Fluid Mech.*, **386**, 281–304. Find this article online

Keller W. C., and J. W. Wright, 1975: Microwave scattering and the straining of wind-generated waves. *Radio Sci.*, **10**, 135–147. Find this article online

Longuet-Higgins M. S., 1960: Changes in the form of short gravity waves on long waves and tidal currents. *J. Fluid Mech.*, **8**, 565–585. Find this article online

Longuet-Higgins M. S., 1963: The generation of capillary gravity waves by steep gravity waves. *J. Fluid Mech.*, **16**, 138–159. Find this article online

Longuet-Higgins M. S., 1992: Capillary rollers and bores. *J. Fluid Mech.*, **240**, 659–679. Find this article online

Longuet-Higgins M. S., 1995: Parasitic capillary waves: A direct calculation. *J. Fluid Mech.*, **301**, 79–107. Find this article online

Perlin M., H. Lin, and C.-L. Ting, 1993: On parasitic capillary waves generated by steep gravity waves: An experimental investigation with spatial and temporal measurements. *J. Fluid Mech.*, **255**, 597–620. Find this article online

Sun S. C., and J. Wu, 1984: On airflow boundary layer above the profile of long waves. *J. Phys. Oceanogr.*, **14**, 1811–1815. Find this article online

Thompson D. R., 1988: Calculation of radar backscatter modulation from internal waves. *J. Geophys. Res.*, **93**, 12371–12380. Find this article online

Thompson D. R., and R. F. Gasparovic, 1986: Intensity modulation in SAR images of internal waves. *Nature*, **320**, 345–348. Find this article online

Tseng R. S., 1987: Longitudinally-averaged and wave-modulated turbulent boundary layers above and below a wind-disturbed water surface. Ph.D. dissertation, University of Delaware, Lewes, DE, 192 pp.

Wright J. W., 1966: Backscattering from capillary waves with application to sea clutter. *IEEE Trans. Antennas Propag.*, **AP-14**, 749–754. Find this article online

Wright J. W., 1968: A new model for sea clutter. *IEEE Trans. Antennas Propag.*, **AP-16**, 217–223. Find this article online

Xu D., P. A. Hwang, and J. Wu, 1986: Breaking of wind-generated waves. *J. Phys. Oceanogr.*, **16**, 2172–2178. Find this article online

Zaneveld J. R. V., E. Boss, and A. Barnard, 2001a: Influence of surface waves on measured and modeled irradiance profiles. *Appl. Opt.*, **40**, 1442–1449. Find this article online

Zaneveld J. R. V., E. Boss, and P. A. Hwang, 2001b: The influence of coherent waves on the remotely sensed reflectance. *Opt. Express*, **9**, 260–266. Find this article online

---

APPENDIX A

5. Deriving the Surface Elevation from Slope Measurements

The surface slope and surface displacement are closely related. The wave displacement record can be derived from the time series of the slope data through the formula

$$\eta = \int \eta_x \, dx \approx \int \eta_x (C \, dt). \qquad \text{(A1)}$$

The formula is expected to work well when the slope signal is produced by a dominant sinusoidal wave train, such as the background waves generated by a mechanical wave generator. For the eight wind conditions presented in this paper, one wave record (wind condition 0, mechanical waves only) is missing and has to be reconstructed from the slope record. The slope data from the last scanning position, which is at the same wind fetch of the wave gauge with 0.02-m crosswind offset, are used to calculate the surface displacement. The procedure is applied to all eight wind conditions. The results are shown as dashed curved in Fig. A1. For the seven wind conditions with the displacement records measured by the wave gauge, the agreement of slope-derived and gauge-measured results (dotted curves) is excellent at low wind conditions and satisfactory at high winds. The missing record is for mechanical waves only and it is judged that the displacement time series derived from the slope data is reliable.

APPENDIX B

6. Resonant Condition for the Occurrence of Parasitic Capillary Waves

Once the capillary waves are generated by the localized surface tension force near the crest of a steep wave, they become free waves and propagate at a speed different from that of the gravity wave that generated them. The phase speed c and group speed c_g of surface waves influenced by gravity and surface tension are

$$c = \left(\frac{g}{k} + \tau k \right)^{1/2}, \qquad \text{(B1)}$$

$$c_g = \frac{g + 3\tau k^2}{2(gk + \tau k^3)^{1/2}}, \qquad \text{(B2)}$$

where g is the gravitational acceleration and τ is the dynamic surface tension. In suitable conditions, the speeds of the generated capillary waves and the generating gravity waves are very close and the two wave systems will propagate together forming a phase-locked system—the parasitic capillary waves. The capillary waves can stay near the crest of the gravity waves that generate them under the condition that either the phase speed or the group speed of the capillary wave matches the phase speed of the gravity wave. Figures B1a,b plot c and c_g as functions of wavelength λ and wave period T, respectively. Because the phase speed of surface wave is not a monotonic function of wavenumber but has a minimum where gravity and surface tension exert equal influence as the restoring forces (occurring at $\lambda_m = 0.017$ m for $\tau = 7 \times 10^{-5}$ N m^{-2} kg^{-1}), resonant propagation may occur if the gravity wave is longer than λ_m and the generated capillary waves are shorter than λ_m.

Another consideration is the dissipation rate of capillary waves, which increases with the wavenumber squared. The modulus of decay, τ_v, defined here as the time that the wave spectral density decreases by e fold, is

$$\tau_v = \frac{1}{4\nu k^2}, \qquad \text{(B3)}$$

where ν is the dynamic viscosity. Using the value 1.146×10^{-6} m^2 s^{-1}, corresponding to the viscosity of water at 15°C, the decay time for short waves is plotted in Fig. B2. For $\lambda = 1 \times 10^{-3}$ m, $\tau_v = 5.5 \times 10^{-3}$ s or about four cycles of the capillary waves, which corresponds to 4×10^{-3} m in distance for the spectral density to attenuate by e fold. For $\lambda = 1 \times 10^{-2}$ m, the e-fold decay distance is 0.135 m.

Both laboratory and field measurements of the surface wave spectrum of short waves have shown that the spectral densities of waves a few millimeters and shorter decrease sharply. The spectral densities, $\chi(k)$, of short waves measured in the field are proportional to k^{-5} in the range of $900 < k < 1600$ rad m^{-1}, and k^{-3} in the range of $100 < k < 900$ rad m^{-1} (Hwang et al. 1996). In the laboratory, the spectral slope in the capillary region is found to be even steeper, Hwang et al. (1993) report k^{-6} in the capillary region and a similar sharp dropoff of the spectral density in the capillary region is reported by Jahne and Riemer (1990). Note that the spectral notation, $S(k)$, used in Hwang et al. (1993) and Jahne and Riemer (1990) differs from $\chi(k)$ used here and in Hwang et al. (1996) by a factor k. The two are related by

$$\langle \eta^2 \rangle = \int \chi(k)\, dk = \int S(k) k\, dk. \qquad \text{(B4)}$$

Theoretical calculations (Longuet-Higgins 1995) and laboratory observations (Cox 1958; Ebuchi et al. 1987) suggest that gravity waves from 0.05 to 0.1 m are most efficient in producing parasitic capillary waves.

APPENDIX C

7. A Discussion of the Ambient Motion

The small disturbances observed in the absence of wind (wind condition 0) raise the question about whether these perturbations are above the noise level of the scanning laser slope gauge. As mentioned in Hwang et al. (1993), one dataset without wind disturbance was collected in the wind-wave-only experiment sequence. The wavenumber spectrum of this dataset represents the ambient noise of the sensor system. In Fig. C1, the spectra of eight wind conditions of the mechanical wave sequence are plotted together with the ambient spectrum. The signal levels of the mechanical wave sequence are significantly higher than that of the ambient condition. The small-scale perturbations noticed in wind condition 0 (mechanical wave only) appear in the neighborhood of $k = 400$ and 800 rad m^{-1}. The signal levels at the two local peaks are about 50 times higher than the spectral densities of the ambient spectrum at the corresponding wavenumbers. This gives confidence that the observed perturbation on the upstream quadrant of the mechanical wave is not an artifact.

Close examination of the ambient spectrum reveals that small-scale perturbations occur on the visually calm water surfaces. The wavelengths of the local spectral peaks are in the 8- to 9-mm range. These small-scale perturbations are also observed in the spectra of low wind cases, detectable up to wind condition 2 (reference wind speed 3.47 m s^{-1}), prior to significant visual breaking of the wind wave field (Fig. C1). In the presence of mechanical waves, these ambient perturbations become organized motion and they are amplified significantly in the divergent phase of the mechanical wave train. This result is conceptually consistent with the relaxation theory (e.g., Hwang and Shemdin 1990; Hwang 1999).

Figures

Click on thumbnail for full-sized image.

FIG. 1. The space–time series of surface slopes measured by a scanning slope sensor, showing the temporal and spatial evolution of small-scale waves. Wind friction velocities for the eight images (labeled from 0 to 7) are 0, 0.11, 0.18, 0.26, 0.33, 0.45, 0.55, and 0.68 m s^{-1}. Simultaneously measured surface displacement from a capacitance wave gauge placed at the downstream end of the scanning segment is plotted at the upper edge (the downstream end of the scanning segment) of each image. For reference, the background wave is properly phase-shifted and plotted at the bottom edge of each image. The short linear segments plotted at $t \approx 1, 3, \ldots$;th, 9 s have a slope corresponding to the phase speed C of the background waves. Using these references, it is easy to see that the propagation speeds of the packets of small waves are mostly slower than C

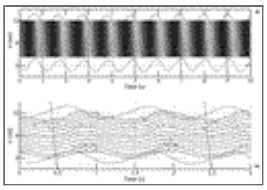

Click on thumbnail for full-sized image.

FIG. 2. Enlarged (top) space–time image and (bottom) waterfall plot of the surface slope for the case of mechanical waves only (wind condition 0). The slope data clearly show the evolution of small and periodic disturbances on the upstream phase of the background wave crests

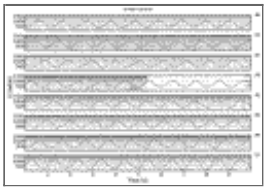

Click on thumbnail for full-sized image.

FIG. 3. The temporal evolution of the wavenumber spectrum of small-scale waves ($60.4 < k < 1571$ rad m^{-1}). The surface displacement data of background waves are plotted at the middle of each image for visual reference of the phase distribution

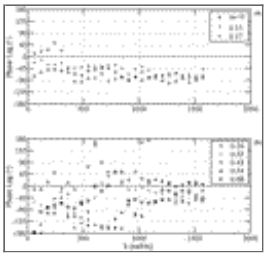

Click on thumbnail for full-sized image.

FIG. 4. The phase lag of maximal cross correlation between the surface displacement of background waves and individual wavenumber components of surface slopes: (a) three cases prior to wave breaking and (b) five cases with wave breaking

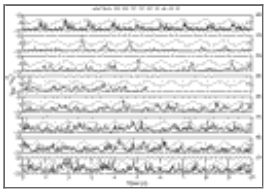

Click on thumbnail for full-sized image.

FIG. 5. The mean square slopes integrated from the slope spectra, plotted together with the surface displacements of background waves. For purpose of illustration, the mean square slope is amplified to fit into the plotting area

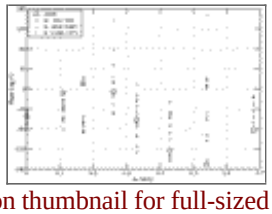

Click on thumbnail for full-sized image.

FIG. 6. The phase lag of maximal cross correlation between the surface displacement of background waves and surface roughness in terms of mean square slopes and individual wavenumber components (see legend for symbols)

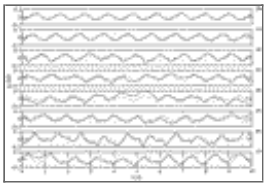

Click on thumbnail for full-sized image.

FIG. A1. A comparison of the surface displacement measured by a capacitance wave gauge (dotted curves) and those derived from the surface slope time series (dashed curves)

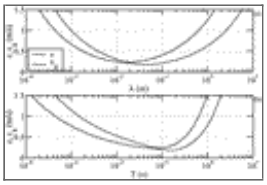

Click on thumbnail for full-sized image.

FIG. B1. The phase and group velocities as functions of (a) wavelength and (b) wave period

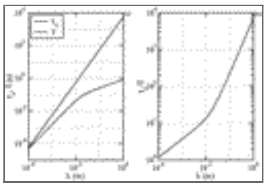

Click on thumbnail for full-sized image.

FIG. B2. (a) The decay timescale τ_v (upper curve) of spectral density attenuation due to viscosity, presented as a function of wavelength. For comparison, the corresponding wave period T (lower curve) is also shown. (b) The ratio τ_v/T

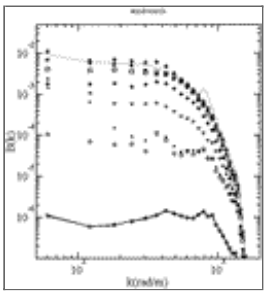

Click on thumbnail for full-sized image.

FIG. C1. The spectrum of ambient condition (connected circles), plotted together with those of the eight wind conditions discussed in the paper. Symbols circle, cross, plus, asterisk, square, pentagon, hexagon, and dotted curve represent wind conditions from 0 to 7

* U.S. Naval Research Laboratory Contribution Number JA/7330—01-0083.

Corresponding author address: Dr. Paul A. Hwang, Oceanography Division, Naval Research Laboratory, Stennis Space Center, MS 39529-5004.
E-mail: paul.hwang@nrlssc.navy.mil

top